

AHDGAN: An Attention-Based Generator and Heterogeneous Dual-Discriminator Generative Adversarial Network for Infrared and Visible Image Fusion

Guosheng Lu¹, Zile Fang¹, Chunming He², Zhigang Zhao¹,

¹College of New Materials and New Energies, Shenzhen Technology University, Shenzhen, 518118, China,

²Shenzhen International Graduate School, Tsinghua University, Shenzhen, 518055, China

Abstract

Infrared and visible image fusion (IVIF) aims to preserve thermal radiation information from infrared images while integrating texture details from visible images. This process enables the capture of important features and hidden details in complex scenes and disturbed environments. The differences that infrared images primarily express thermal radiation through image intensity while visible images mainly represent texture details via image gradients, has long been considered a significant obstacle to IVIF technology development. Existing dual-discriminator Generative Adversarial Networks (GANs) use two identical discriminators to guide the model in learning different types of information. However, given the intrinsic differences between infrared and visible images, using two heterogeneous discriminators is more effective. This paper proposes a novel attention-based generator and heterogeneous dual-discriminator generative adversarial network (AHDGAN) for infrared and visible image fusion. Specifically, the model employs two structurally different discriminators to address the distinct learning needs of infrared and visible image information. These include a global discrimi-

nator for thermal radiation information and a Markovian discriminator for detailed information. Additionally, different multi-scale attention modules are introduced to help the discriminators focus better on their respective source images. Based on this, to integrate the learned information from different source images effectively, an attention mechanism is designed in the generator to construct an information fusion layer. This approach guides the model to learn thermal radiation information from infrared images while simultaneously capturing texture details from visible images. Extensive experiments on various public datasets demonstrate the superiority of our proposed AHDGAN over other state-of-the-art (SOTA) algorithms, highlighting its enhanced potential for practical applications.

Keywords: Infrared and visible image, Generative adversarial network, Attention mechanism.

1. Introduction

Infrared and visible image fusion (IVIF) is one of the prominent areas of convergence, providing superior complementarity to images produced by both sensors [1–4]. Infrared sensors capture thermal radiation information emitted by objects, effectively emphasizing significant target areas even in challenging environmental conditions such as overexposure, low illumination, and obstruction. However, these images typically exhibit lower spatial resolution. In contrast, visible sensors acquire reflected light information, yielding images with higher spatial resolution capable of characterizing effective information in complex scenes. Nevertheless, visible images are susceptible to changes in external conditions such as weather and illumination. Fusion of these two image types can effectively compensate for their respective deficiencies, enabling fused results to convey rich and crucial information in harsh environments and complex scenes. Fig. 1 illustrates the benefits of IVIF, underscoring its high potential for practical engineering applications [4, 5].

In recent decades, a variety of approaches to image fusion have emerged, and they are typically classified into two categories: traditional model-based



Fig. 1. Example of the effect of IVIF.

methods and deep learning-based methods.

Traditional model-based methods commonly fall into four categories: multi-scale transform methods (MST) [6–8], sparse representation (SR) [9, 10], subspace methods [11], and hybrid techniques [12, 13]. Despite their ability to yield satisfactory results, traditional methods suffer from inherent limitations. Specifically, manually designed feature extraction operators and fusion rules often fail to capture image features comprehensively.

Conversely, deep learning has gained prominence in image fusion tasks due to the robust data representation capabilities of neural networks. Primary deep learning-based fusion methods include convolutional neural network (CNN) models [14–18], auto-encoder (AE) architectures [19–22], and generative adversarial network (GAN) methods [23–28]. However, in the absence of ground truth or standard fused images, GAN methods, which guide model learning with source images, can perform better.

In the realm of GAN methods, Ma et al. proposed DDcGAN [24] tailored for the multi-source fusion domain in 2020, garnering significant attention. On this foundation, many dual-discriminator GAN models have been proposed [4, 26–30], all showing remarkable fusion performance.

Nevertheless, we have identified some neglected aspects. On the one hand, there are variations in how information is represented between different source images, yet existing dual-discriminator GAN methods overlook this issue. Instead, they employ discriminator networks with identical de-

signs, encouraging the model to learn different features. On the other hand, current methods primarily concentrate on minimizing information loss during extraction, which is indeed important. However, it is equally crucial to efficiently integrate the extracted information from various sources.

To address these shortcomings, this paper introduces AHDGAN. Firstly, considering the distinct characteristics of infrared and visible images, a structurally diverse dual-discriminator network is designed to enhance the model’s learning capabilities. The global discriminator targets image region information to capture thermal radiation features, while the Markovian discriminator focuses on local detail information to extract texture details from visible images. Secondly, a fusion strategy is incorporated into the generator, utilizing an attention network that assigns weights to features based on pixel disparities, thereby achieving effective fusion and comprehensive information representation.

The contributions of this work are summarized below:

- (1) A novel heterogeneous dual-discriminator network is proposed to improve the model’s learning capabilities. The global discriminator, featuring a multi-scale channel attention module, is designed to foster comprehensive learning of thermal radiation information, while the Markovian discriminator, incorporating a multi-scale spatial attention module, is designed to enhance the capture of detailed texture information. This innovative design adapts to the unique characteristics of infrared and visible images, enabling targeted and concurrent learning of both thermal radiation and texture details.
- (2) The generator introduces a new attention-based fusion strategy that utilizes the disparities between source images to integrate the acquired image information. This approach ensures that the fusion results effectively highlight the features learned from different sources.
- (3) Comprehensive experiments are conducted on various public datasets. Both qualitative and quantitative comparisons with other SOTA algorithms on three widely used infrared and visible image datasets demonstrate the superior performance of our method. Moreover, comparisons

regarding resistance to degradation, analyses of downstream applications, and extension experiments validate the significant potential of the approach for practical applications.

The subsequent sections of this paper are organized as follows: Section 2 provides an overview of traditional IVIF technology and deep learning-based IVIF technology, with a particular focus on the application of GANs in this field. In Section 3, we delve into the structure of the proposed model and elaborate on its advantages. Section 4 presents numerous experimental validations, encompassing qualitative and quantitative analyses, ablation experiments, degradation resistance comparisons, downstream application evaluations, and extended experiments. Finally, conclusions are drawn in Section 5.

2. Related works

2.1. Model-Based IVIF

Model-based IVIF methodologies prioritize the design of feature extraction operators and fusion rules to attain desired outcomes. As previously delineated, these methods can be classified into four primary categories. The first category comprises MST-based methods, which are theoretically grounded in the notion that an image can be dissected into distinct components owing to the varied scales of different features. Satisfactory fusion results are achieved by integrating these components through designed rules. Representative studies include pyramid transform [6], wavelet transform [8], and curvelet transform [31]. The second category comprises SR methods. Given the observation that visual recognition systems process images in a sparse manner, enhancing valid information representation is feasible by learning an over-complete dictionary and characterizing image features with sparse coefficients [32, 33]. The third category encompasses subspace-based fusion methods. Recognizing the redundancy present in most images, some scholars propose capturing internal structural information by mapping images to a low-dimensional subspace to eliminate interference from this re-

dundant information effectively [11, 34]. The fourth category involves hybrid methods, devised to bolster fusion performance by amalgamating the advantages of the aforementioned methods [12, 35]. Additionally, novel perspectives in IVIF have emerged, such as GTF [36] proposed by Ma et al. in 2016, rooted in the theory of Total Variation (TV).

2.2. Deep Learning-Based IVIF

Compared to traditional methods that rely on manually designed rules, deep learning-based algorithms harness the potent fitting capability of neural networks. This renders them superior and has consequently garnered significant attention in the image fusion field.

1) *CNN and AE for IVIF*: The CNN methods utilize convolutional neural networks to extract features from images, enhancing the fusion process and improving image quality. Within the CNN-based framework, Liu et al. introduced a multi-focus fusion strategy in 2017 [37], facilitating fusion tasks by learning the mapping between source images and focus maps. Li et al. utilized a pre-trained ResNet-50 model to extract deep features from images [38]. Zhang et al. employed sequential convolutional layers to extract features and enrich fusion results with information [18].

The AE methods utilize autoencoders to learn the compact representation of images and reconstruct the original data, aiming to extract low-dimensional features and information from the images. Regarding AE-based algorithms, Li et al. proposed a novel codec model in 2018 [19], leveraging dense connections in the encoder to enhance information utilization. Li et al. achieved feature reuse through a multi-scale approach by focusing on features at varying scales [39]. Wang et al. innovatively combined the strengths of these two AE models to aggregate useful features from both horizontal and vertical directions simultaneously [22].

2) *Dual-Discriminator GAN for IVIF*: The GAN methods learn to generate realistic image samples by utilizing source images to guide the model during training. In 2020, Ma et al. proposed DDcGAN [24], characterized by two discriminators with identical structures, aimed at compelling the generator

to learn detailed features from visible images and thermal radiation information from infrared images. In 2021, Li et al. introduced AttentionFGAN [26], incorporating multi-scale attention structures in both generator and discriminators to glean more information about salient regions from source images. Zhang et al. proposed GAN-FM [4], which learns richer information through improved discriminator structures. Diverging from conventional global discriminator architectures, it integrates a Markovian discriminator to enhance focus on local image block structures. In 2022, Liu et al. presented TarDAL [28], employing a joint training strategy for downstream detection tasks, achieving bilevel optimization between fusion and detection. In 2023, Zhou et al. devised SDDGAN [40], which is a semantic-supervised fusion network capable of preserving features of crucial semantic objects in images to learn richer important information.

However, existing dual-discriminator GAN methods share a unified structure for the two discriminators, which inevitably overlooks a critical issue: due to the disparate imaging mechanisms between infrared and visible images, the thermal radiation information in infrared images is primarily manifested as image intensity, while the texture details in visible images are expressed through image gradients. Consequently, discriminators with uniform structures cannot effectively guide the generator to learn features targeted from different source images, resulting in the inevitable loss of valuable information.

3. Method

3.1. Framework Overview

In this paper, a novel AHDGAN is proposed, and the overall framework is depicted in Fig. 2. This model comprises two networks: the generator network and the dual-discriminator network. The generator is designed as a multi-scale skip-connected codec structure to realize the information extraction, fusion, and image reconstruction. Two discriminators are defined as different structures to learn thermal region and texture detail informa-

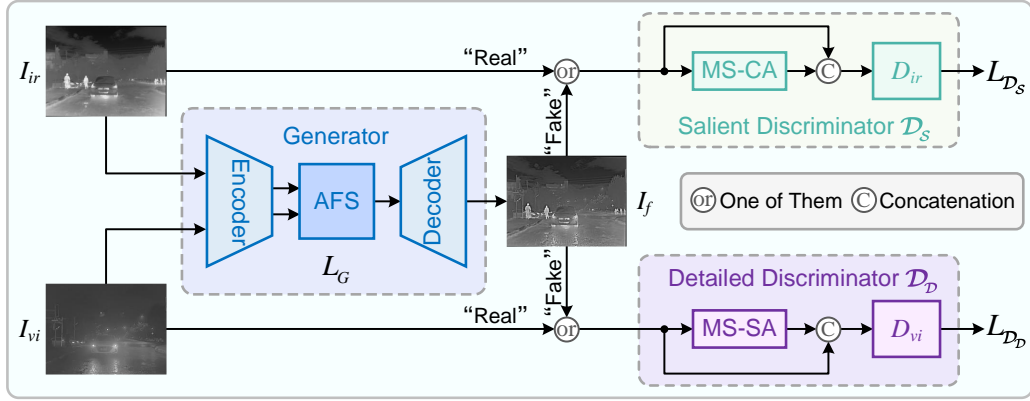


Fig. 2. The framework of the proposed AHDGAN. AFS, MS-CA, and MS-SA are short for attention-based fusion strategy, multi-scale channel attention, and multi-scale spatial attention, respectively.

tion, respectively, which are the saliency discriminator (\mathcal{D}_S) targeting infrared images and the detailed discriminator (\mathcal{D}_D) focusing on visible images.

3.2. Architecture of Generator

Inspired by Nestfuse [39], we design the generator as a multi-scale skip-connected structure to utilize image information effectively. As depicted in Fig. 3, the generator consists of three sub-networks: encoder, AFS, and decoder.

1) *Encoder and Decoder in Generator:* The encoder and decoder sub-networks primarily consist of the convolutional block (CB), encoder block (EB), and decoder block (DB). CB contains one convolutional layer, EB denotes two convolutional operations with different kernel sizes, and DB consists of two identical convolutional layers. Specifically, after importing the source images I_{ir} and I_{vi} into the encoder sub-network, deep feature maps F_{ir}^k and F_{vi}^k with different sizes are obtained respectively through the CB, EB, and down-sampling operations. Here, k represents the scale level of the feature maps. Subsequently, after traversing the fusion strategy sub-network, the fused deep feature F_{fused}^k is produced. Ultimately, the final fused image I_f is generated after a series of up-sampling and DB operations in the decoder sub-network. The sampling operations within the network are used to

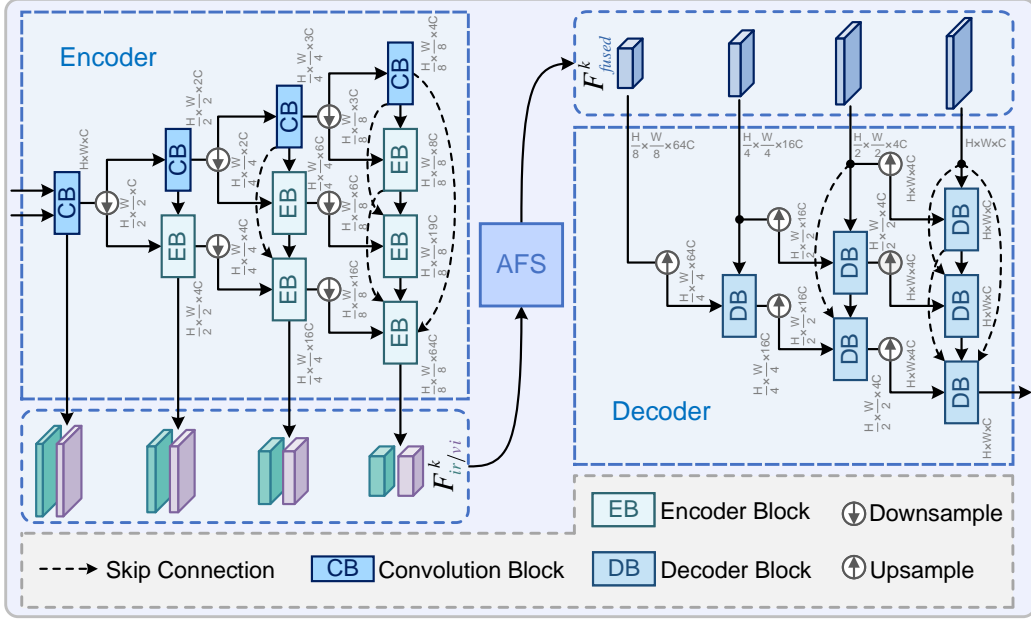


Fig. 3. Detailed structure of the generator.

utilize multi-scale features, while the skip connections serve to enhance the extraction and preservation of intermediate features.

2) *AFS in Generator:* It is a noteworthy challenge to fuse the information from different source images effectively, particularly the important thermal radiation and critical detail information. Moreover, AHDGAN uses disparate dual-discriminators to guide the generator to learn distinct features separately. Therefore, it is necessary to consider the potential issue of representation imbalance that may arise after fusing the separately learned information simultaneously. To address these issues, we develop AFS as the information fusion layer to integrate the information rationally and effectively. The detailed structure is shown in Fig. 4.

From the regions boxed in Fig. 1, it can be observed that the larger the differences between corresponding regions of the source images, the more important the specific information of the corresponding source images becomes. Hence, it is logical to represent the different importance of these pieces of information based on the distance between the source images, and then allocate corresponding weights accordingly. The formula for calculating the

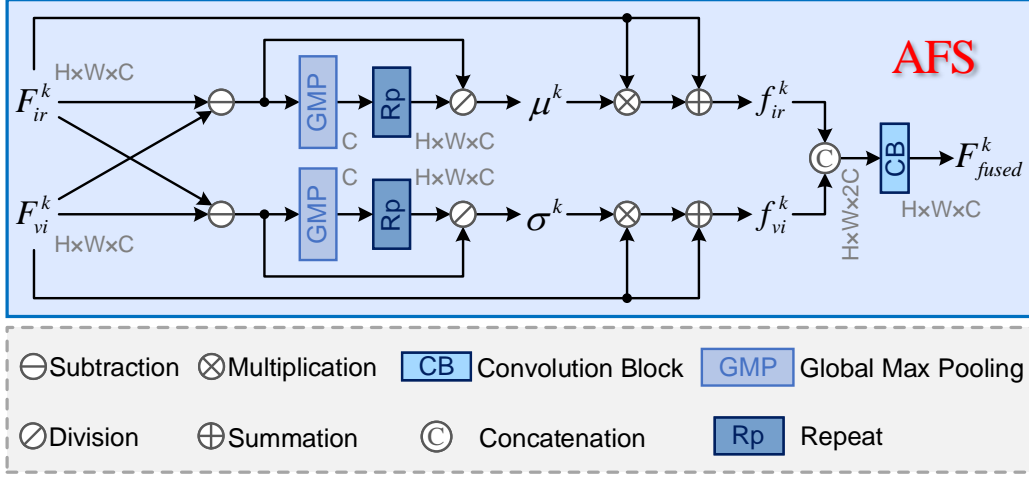


Fig. 4. Construction of AFS.

weighting coefficients is as follows:

$$\mu^k = \frac{F_{ir}^k - F_{vi}^k}{Rp(GMP(F_{ir}^k - F_{vi}^k))} \quad (1)$$

$$\sigma^k = \frac{F_{vi}^k - F_{ir}^k}{Rp(GMP(F_{vi}^k - F_{ir}^k))} \quad (2)$$

where $Rp(\cdot)$ and $GMP(\cdot)$ donate repeat and global max pooling, respectively. Following these computations, both μ^k and σ^k reflect the importance of different information in feature maps, with values falling into three categories: positive, negative, and zero. The positive values indicate that the information in the subtracted image is relatively significant and needs to be strengthened, the negative values need to be weakened, and the zero values remain unchanged.

Subsequently, the feature maps that can emphasize the respective important information are calculated through the following formulas:

$$f_{ir}^k = \mu^k * F_{ir}^k + F_{ir}^k \quad (3)$$

$$f_{vi}^k = \sigma^k * F_{vi}^k + F_{vi}^k \quad (4)$$

where $*$ is the multiplication operation.

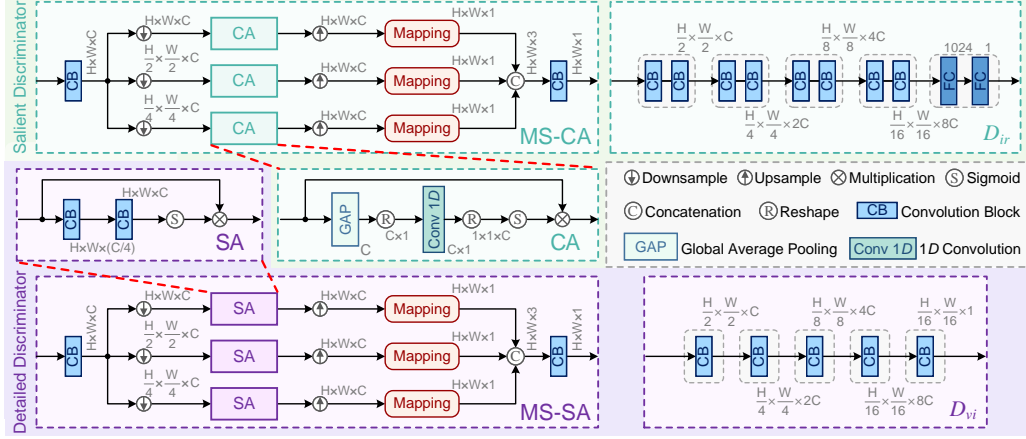


Fig. 5. Details of discriminator networks.

Eventually, the fused features F_{fused}^k are obtained after passing through the concatenation operation ($concat(\cdot)$) and then the convolutional layer ($conv(\cdot)$):

$$F_{fused}^k = conv(concat(f_{ir}^k, f_{vi}^k)) \quad (5)$$

The final acquired deep features maps F_{fused}^k integrate the information from different source images reasonably, effectively alleviating the problem of the unbalanced information representation in the fusion results.

3.3. Architecture of Discriminators

In the AHDGAN proposed in this paper, the discriminator networks are composed of two parts: the salient discriminator and the detailed discriminator. The specific architecture is displayed in Fig. 5. The input images are first fed into the multi-scale attention modules (MS-CA and MS-SA) respectively to compute the corresponding attention maps. Then, concatenate these maps with input images accordingly and feed them into the corresponding discriminative modules (D_{ir} and D_{vi}).

1) *Salient Discriminator*: To facilitate the generator to focus on learning thermal region information from infrared images during adversarial training, the sub-network is split into two components: the MS-CA and the infrared discriminative module (D_{ir}). The role of D_{ir} is to distinguish between the

fused output and the original infrared image, and it consists of five layers. The first four layers are all two identical convolution operations and the last layer includes two fully connected operations. After passing through this module, the result of the discrimination (the final determine probability of the input image) is produced. Furthermore, to restrict the discriminator to concentrate on the most critical thermal regions in the infrared image during training, the MS-CA structure is introduced. Firstly, Recognizing that single-scale features may not capture all essential thermal radiation information, a multi-scale mechanism is adopted to utilize more deep features via down-sampling. Additionally, to focus on the distribution of the overall pixels in the image, i.e., the intensity information of the thermal region, the channel attention module (CA) [41] is constructed to calculate the weight values of different channels through global average pooling (GAP) and 1-dimensional convolution, thus reweighting the global information of the infrared features. Then, the images are restored to their original size with up-sampling operations, and weighted maps are computed after the mapping operation (selecting the maximum value of all features in channel dimensions [42]). Finally, these images are concatenated to form the ultimate attention map. As we can see, our salient discriminator targeted at thermal region information in the infrared image can effectively guide the generator in learning infrared features.

2) *Detailed Discriminator*: Different from the global discriminative structure used in salient discriminator, to encourage the generator to learn the detailed information of visible images fully, the Markovian discriminative network [43] is adopted in the visible discriminative module (D_{vi}). This network can classify each block of the input image, focusing on local details. As shown in Fig. 5. It consists of five convolution layers, and the output is a matrix that can be averaged to obtain the final determine probability. Additionally, in line with MS-CA, the MS-SA is also integrated into the detailed discriminator, differently, to emphasize the information of important local details in a better way, the relationship between local pixels is modeled using

the spatial attention (SA) [44], which can capture more relationships between pixel spaces by downscaling and upscaling the number of channels during two convolutions, thereby giving greater weight to critical spatial structure information. For this reason, the generator facilitates more efficient preservation of texture details during adversarial learning.

3.4. Loss Function

As depicted in Fig. 2, the loss function is comprised of two parts: the loss function of the generator (L_G), and the loss function of discriminators ($L_{\mathcal{D}_S}$ and $L_{\mathcal{D}_D}$).

1) *Loss Function of Generator:* In order to force the generated image to contain sufficient information from both the infrared and visible images, the loss function used to guide the training of the generator consists of the adversarial loss (L_{adver}) and the basic loss (L_{basic}):

$$L_G = L_{adver} + \alpha L_{basic} \quad (6)$$

where α is the parameter to control the two terms.

Adversarial Loss L_{adver} . Considering that the generator needs to deceive both discriminators during training, the adversarial loss can be defined as follows:

$$L_{adver} = \mathbb{E}_{I_f \sim d_{I_f}} [(\mathcal{D}_S(I_f) - \phi)^2] + \mathbb{E}_{I_f \sim d_{I_f}} [(\mathcal{D}_D(I_f) - \phi)^2] \quad (7)$$

where \mathbb{E} represents the mathematical expectation, \mathcal{D}_S and \mathcal{D}_D stand for the two discriminators, I_f denotes the fused image and d_{I_f} is its distribution. Moreover, ϕ refers to a probability label (the discriminative probability of discriminators for the generated image) and is set to 1 because the generator expects the discriminators to be unable to distinguish between images.

Basic Loss L_{basic} . The purpose of L_{basic} is to constrain the learning of valid information in source images, and is divided into two items: the learning of thermal radiation information and the learning of texture detail information:

$$L_{basic} = L_{visible} + \beta L_{infrared} \quad (8)$$

The equations for $L_{infrared}$ and $L_{visible}$ are as follows:

$$L_{infrared} = \|I_f - I_{ir}\|_F^2 \quad (9)$$

$$L_{visible} = \|\nabla(I_f) - \nabla(I_{vi})\|_1 \quad (10)$$

where β controls the trade-off between the infrared image and visible image, $\nabla(\cdot)$ is the Sobel gradient operator known for its better ability to resist interference, $\|\cdot\|_F^2$ and $\|\cdot\|_1$ denote the Frobenius norm and ℓ_1 norm.

2) *Loss Function of Discriminators:* The loss function of discriminators L_D is combined by the loss $L_{\mathcal{D}_S}$ of the salient discriminator and the loss $L_{\mathcal{D}_D}$ of the detailed discriminator. Since AHDGAN has two heterogeneous discriminators that may aggravate the imbalance conflict when the generator learns different features, we jointly train the loss of the infrared and visible discriminators instead of calculating them separately [26]. The weight parameter γ is introduced to allow the model to adjust the optimization to solve the training imbalance arising from the difference of the discriminative structure:

$$L_D = L_{\mathcal{D}_D} + \gamma L_{\mathcal{D}_S} \quad (11)$$

The equations for $L_{\mathcal{D}_S}$ and $L_{\mathcal{D}_D}$ are as follows:

$$\begin{aligned} L_{\mathcal{D}_S} = & \frac{1}{2} \times \mathbb{E}_{I_{ir} \sim d_{I_{ir}}} [(\mathcal{D}_S(I_{ir}) - \xi_1)^2] \\ & + \frac{1}{2} \times \mathbb{E}_{I_f \sim d_{I_f}} [(\mathcal{D}_S(I_f) - \xi_2)^2] \end{aligned} \quad (12)$$

$$\begin{aligned} L_{\mathcal{D}_D} = & \frac{1}{2} \times \mathbb{E}_{I_{vi} \sim d_{I_{vi}}} [(\mathcal{D}_D(I_{vi}) - \zeta_1)^2] \\ & + \frac{1}{2} \times \mathbb{E}_{I_f \sim d_{I_f}} [(\mathcal{D}_D(I_f) - \zeta_2)^2] \end{aligned} \quad (13)$$

where I_{ir} denotes the infrared image and $d_{I_{ir}}$ is its distribution, while I_{vi} denotes the visible image and $d_{I_{vi}}$ is its distribution. The probability labels ξ_1 and ξ_2 are set to 1 and 0, respectively, and ζ_1 and ζ_2 are similarly set to 1 and 0, respectively. This is because the discriminators expect to distinguish the input image as accurately as possible (giving the probability value of the real image as large as possible as well as the probability value of the generated image as small as possible).

3.5. Discussion

Since the utilization of heterogeneous discriminant structures has not been considered in previous dual-discriminator models, we justify the proposed AHDGAN in the following three aspects:

1. The dual-discriminator GAN is mainly used to address the characteristics of multiple source images in the image fusion area. Based on this, considering that what needs to be learned from infrared images is intensity information, while what needs to be learned from visible images is gradient information, it is logical to devise two heterogeneous discriminator networks, respectively, in this paper to learn the features of different source images. Additionally, this study aims to bring some inspiration.

2. The rationality of AHDGAN is manifested in the overall performance of the model and the effectiveness of the key heterogeneous discriminator networks. So following the experimental content referenced in [45, 46], the qualitative and quantitative experiments are conducted in subsection 4.2 to assess the overall impact of the model. Additionally, the ablation experiments on heterogeneous discriminator networks are done in subsection 4.3 for evaluation.

3. The reasonability of the model is also reflected by its generalization capability, including its performance in practical applications and extended domains. Therefore, in Section 4.4, we compare its degradation resistance capabilities. In Section 4.5, object detection and tracking experiments are conducted. Furthermore, in Section 4.6, extended fusion experiments in the biomedical field are performed.

4. Experiment

4.1. Implementation Details

1) Datasets: The experiments are conducted on three public datasets: RoadScene [14], LLVIP [47], and M^3FD [28]. The RoadScene dataset comprises 221 pairs of infrared-visible images depicting various traffic scenes. LLVIP contains traffic images captured in low-light conditions, from which

Table 1

Details of datasets division.

Datasets	Training Set	Testing Set	Total
RoadScene	181	40	221
LLVIP	100	200	300
M^3FD	100	200	300

we select 300 pairs for our experiments. Additionally, M^3FD is a newly available multi-scene multimodal dataset consisting of 300 pairs of images. We randomly partition the datasets into training and testing sets, with details presented in Table 1. Subsequently, we uniformly crop the training set into image blocks sized at 128×128 to augment the training images, resulting in a total of 13,903 images.

2) *Comparative Methods*: Our method, AHDGAN, is compared with nine SOTA methods, including a typical traditional method, GTF [36], and eight deep learning-based methods. U2Fusion [14] and STDFusion [48] are CNN-based fusion models, while DeepFuse [49], AUIF [50], and DRF [51] utilize AE-based networks. Additionally, FusionGAN [23], GANMcC [25], and GAN-FM [4] are GAN-based methods. All comparison methods have publicly available code, and we reference the original papers for the corresponding parameter settings. We conduct retraining and testing using the same training and test data as specified in the respective papers.

3) *Evaluation Metric*: Following [52, 53], we employ six commonly used indicators to evaluate the performance of IVIF methods from multiple perspectives. These indicators include entropy (EN) [54], average gradient (AG) [55], spatial frequency (SF) [56], feature mutual information (FMI) [57], visual information fidelity (VIF) [58], and universal image quality index (UIQI) [59]. EN measures the information richness of the fused image, while AG assesses quality based on gradients. SF reflects the rate of grayscale change in the image, and FMI calculates mutual information of image features. VIF evaluates the visual quality of the fused image, and UIQI compares image brightness. In summary, larger values for these metrics indicate better fusion

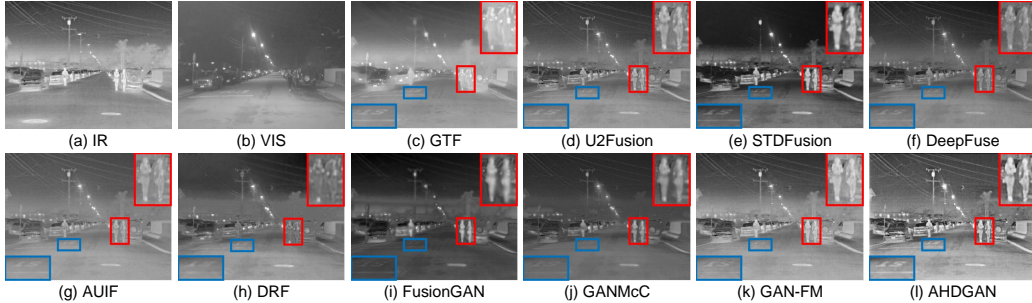


Fig. 6. Qualitative results for RoadScene. (a) and (b) are the infrared image and visible image. (c)-(l) are the fused images processed by the ten comparison methods.

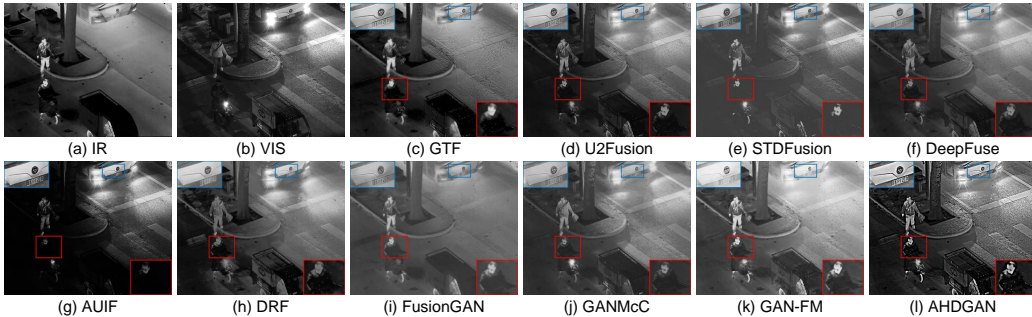


Fig. 7. Qualitative results for LLVIP. (a) and (b) are the infrared image and visible image. (c)-(l) are the fused images processed by the ten comparison methods.

effects.

4) *Training Details:* We utilize TensorFlow and the Adam optimizer in our model. During the training process, the generator and discriminators are updated alternately and iteratively. Specifically, after training \mathcal{D}_D four times and \mathcal{D}_S twice, the generator is trained twice. We set the epochs and batch sizes to 20 and 16, respectively. Additionally, we initialize the learning rate to 2×10^{-4} . Except for GTF, which is executed on MATLAB R2023a, all other methods run on an NVIDIA RTX 2080 Ti GPU. Furthermore, the hyperparameters α , β , and γ in Equations 6, 8, and 11 are set to 100, 5, and 5, respectively.

4.2. Results and Analysis on Public Datasets

1) *Qualitative Comparisons:* To demonstrate the superiority of our model, we qualitatively assess three representative image pairs from the testing set and compare the results with nine SOTA methods mentioned earlier. The

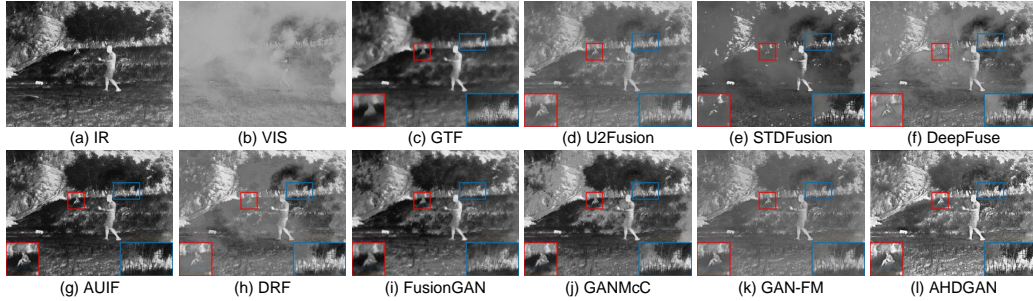


Fig. 8. Qualitative results for M^3FD . (a) and (b) are the infrared image and visible image. (c)-(l) are the fused images processed by the ten comparison methods.

fusion outcomes of AHDGAN and the comparative algorithms are illustrated in Fig. 6 - 8. The primary thermal information, depicted through bright human body regions, and textures, indicated as lane lines, license plates, and bushes, are evaluated. To enhance clarity, we zoom in on a red-framed area for the thermal targets and a blue-framed area for the texture details, placing them in one corner of the picture.

From a visual perspective, AHDGAN exhibits several unique advantages. Firstly, our method closely aligns with the requirements of IVIF by generating fused images with both infrared and visible information. Notably, the results from AHDGAN exhibit similar pixel distributions to infrared images while retaining substantial texture information from visible images. Secondly, AHDGAN excels in capturing more salient thermal region information and clearer detail information compared to other SOTA algorithms, such as pedestrians in the red boxes in Fig. 6 and Fig. 7, and the bushes in Fig. 8. This advantage can be attributed to the two distinct discriminator structures built in this paper, enabling the model to learn more from source images.

Additionally, our method emphasizes critical information beneficial for subsequent practical tasks. This is owed to the addition of MS-CA and MS-SA structures in discriminators, allowing focus on learning essential information. Moreover, the AFS module enables fused images to emphasize important information, as evidenced by the enhanced visibility of hidden persons in Fig. 8, and the lane lines and license plates in Fig. 6 and Fig. 7.

Furthermore, among the nine SOTA methods used for comparison, GTF

Table 2

The average scores of the six metrics in INO, TNO, RoadScene, LLVIP, and M^3FD datasets, with the best two results are in red and blue.

Datasets	Metrics	GTF	U2Fusion	STDFusion	DeepFuse	AUIF	DRF	FusionGAN	GANMcC	GAN-FM	AHDGAN
RoadScene	EN \uparrow	7.499	7.192	7.371	7.141	7.472	7.111	7.048	7.209	7.431	7.293
	AG \uparrow	3.529	5.084	5.149	5.102	5.002	3.550	3.409	3.818	4.801	5.173
	SF \uparrow	9.904	11.531	13.595	12.883	13.646	8.608	8.833	9.122	12.560	14.047
	FMI \uparrow	0.868	0.858	0.858	0.851	0.848	0.839	0.847	0.850	0.861	0.854
	VIF \uparrow	0.229	0.458	0.463	0.442	0.463	0.337	0.274	0.427	0.420	0.465
	UIQI \uparrow	0.844	0.731	0.718	0.807	0.699	0.434	0.720	0.731	0.769	0.860
LLVIP	EN \uparrow	7.126	6.812	5.296	6.924	5.263	6.861	6.365	6.708	7.338	7.695
	AG \uparrow	3.748	3.604	3.177	2.903	2.365	2.041	2.044	2.276	3.082	4.676
	SF \uparrow	13.737	13.388	12.729	9.259	10.847	5.728	7.308	7.432	10.348	15.415
	FMI \uparrow	0.910	0.903	0.904	0.902	0.903	0.899	0.901	0.901	0.903	0.904
	VIF \uparrow	0.405	0.469	0.242	0.431	0.283	0.362	0.206	0.364	0.470	1.001
	UIQI \uparrow	0.785	0.651	0.746	0.848	0.275	0.436	0.769	0.824	0.533	0.694
M^3FD	EN \uparrow	7.225	6.794	6.428	6.728	6.843	6.428	6.639	6.780	7.085	7.511
	AG \uparrow	4.247	4.218	4.239	3.640	4.240	2.411	2.769	2.719	3.671	5.483
	SF \uparrow	12.822	12.645	12.965	10.072	12.881	6.458	8.355	7.654	10.768	16.150
	FMI \uparrow	0.891	0.887	0.888	0.879	0.881	0.871	0.866	0.878	0.874	0.878
	VIF \uparrow	0.349	0.495	0.329	0.445	0.603	0.302	0.211	0.381	0.378	0.890
	UIQI \uparrow	0.721	0.714	0.886	0.807	0.609	0.432	0.806	0.809	0.626	0.814

tends to overlook boundary information (see Fig. 6). U2Fusion strikes a balance that does not enhance either thermal region or texture information significantly (see Fig. 8). STDFusion and AUIF perform poorly in low-light conditions (see Fig. 7). DeepFuse, DRF, GANMcC, and GAN-FM typically lose some important texture features of visible images (see Fig. 6). Additionally, FusionGAN consistently fails to retain high-contrast characteristics similar to infrared images (see Fig. 8).

2) *Quantitative Comparisons:* We further conduct a quantitative comparison of test images from three datasets to assess the effectiveness of AHDGAN. Table 2 presents the average scores for the six metrics described above, with the best values emphasized in red and the next best in blue. It is evident that AHDGAN achieves the highest scores for AG, SF, and VIF across all scenes, demonstrating its superiority in preserving gradient and texture information, and enhancing visual quality. Moreover, AHDGAN also ranks at the top for EN, FMI, and UIQI metrics in most cases, showcasing its excellence in terms

Table 3

Ablation study of the generator structure on RoadScene. The best results are marked in **bold**.

Method	RoadScene					
	EN \uparrow	AG \uparrow	SF \uparrow	FMI \uparrow	VIF \uparrow	UIQI \uparrow
w/o Sampling	7.206	3.513	10.139	0.865	0.084	0.848
w/o Skip Connection	7.148	4.904	13.604	0.850	0.368	0.857
w/o AFS	7.137	3.883	10.500	0.843	0.258	0.863
AHDGAN	7.293	5.173	14.047	0.854	0.465	0.860

Table 4

Ablation study of the generator structure on LLVIP. The best results are marked in **bold**.

Method	LLVIP					
	EN \uparrow	AG \uparrow	SF \uparrow	FMI \uparrow	VIF \uparrow	UIQI \uparrow
w/o Sampling	7.160	3.786	13.359	0.904	0.160	0.613
w/o Skip Connection	7.164	3.444	11.131	0.905	0.561	0.665
w/o AFS	6.968	2.543	8.815	0.903	0.399	0.615
AHDGAN	7.695	4.676	15.415	0.904	1.001	0.694

of information richness, mutual information utilization, and image brightness preservation. While there are some instances where our results are sub-optimal, this could be attributed to variations in scene characteristics across datasets.

4.3. Ablation Experiment

In this subsection, a series of experiments are conducted to validate the efficacy of the AHDGAN structure, comprising two parts: verification of the rationality of the specific structure in the generator, and evaluation of the specific network in the discriminators.

1) *Analysis of the structure of the generator*: Here the ablation experiments on the multi-scale structure, skip connections, and AFS in the generator are performed.

Table 5

Ablation study of the generator structure on M^3FD . The best results are marked in **bold**.

Method	M^3FD					
	EN↑	AG↑	SF↑	FMI↑	VIF↑	UIQI↑
w/o Sampling	7.011	4.101	12.348	0.887	0.070	0.802
w/o Skip Connection	6.932	4.137	12.168	0.878	0.507	0.857
w/o AFS	6.638	2.690	7.904	0.864	0.263	0.854
AHDGAN	7.511	5.483	16.150	0.878	0.890	0.814

Ablation of Sampling. In the generator network, we refer to the multi-scale structure [39] to extract and fuse the deep features of the image. This is realized by sampling operators. So to confirm the effectiveness of this multi-scale structure, we conduct the ablation experiment of sampling operators. In this experiment, we keep other structures and settings unchanged, while the sampling operations are eliminated (w/o Sampling), i.e., the generative network becomes a dense skip-connected structure. Table 3 - Table 5 provide a specific evaluation of the metrics. It can be seen that the multi-scale structure effectively utilizes deep information of the image, except for individual scenarios in FMI.

Ablation of Skip Connections. In order to reduce the information loss during feature extraction and reconstruction, skip connections are also employed in the generator network, so this structure needs to be validated. As indicated in Table 3 - Table 5, the addition of skip connections leads to improved performance across various metrics, and has obvious improvement in EN, AG, SF, and VIF. Thus, the use of skip connections is reasonable.

Ablation of AFS. A novel fusion strategy AFS is also proposed in this paper. AFS can enhance the visual effect of the fused image and help to improve the efficiency of downstream tasks. Here the ablation experiment of AFS is performed, and in Table 3 - Table 5, w/o AFS represents that the fusion strategy proposed is replaced by a simple overlap:

$$F_{fused}^k = 0.5 \times F_{ir}^k + 0.5 \times F_{vi}^k \quad (14)$$



Fig. 9. Discussion of the MS-CA and MS-SA modules on LLVIP.

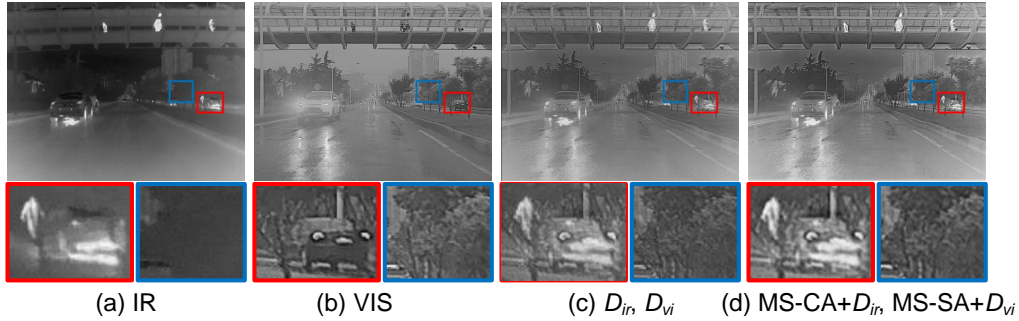


Fig. 10. Discussion of the MS-CA and MS-SA modules on M^3FD .

It can be seen that the proposed AFS module notably boosts the metrics including EN, AG, SF, FMI, and VIF, which effectively improves the information expression capability of the fused image.

2) *Analysis of the structure of discriminators:* In this analysis, we examine the impact of the attention modules MS-CA and MS-SA, as well as the heterogeneous discriminator modules \mathcal{D}_S and \mathcal{D}_D .

Ablation of MS-CA and MS-SA. To prompt the model to learn more information about important thermal regions and key local details, we incorporate MS-CA and MS-SA modules. To justify the effectiveness of these modules, an ablation experiment is conducted. In Fig. 9 and Fig. 10, (a) and (b) represent the infrared image and visible image, respectively. In (c), the result after removing the attention modules is depicted. (d) illustrates the proposed setup of AHDGAN, which includes these attention modules.

Observing method (c), we note that after discarding the attention modules, some thermal radiation and texture information are retained, but the

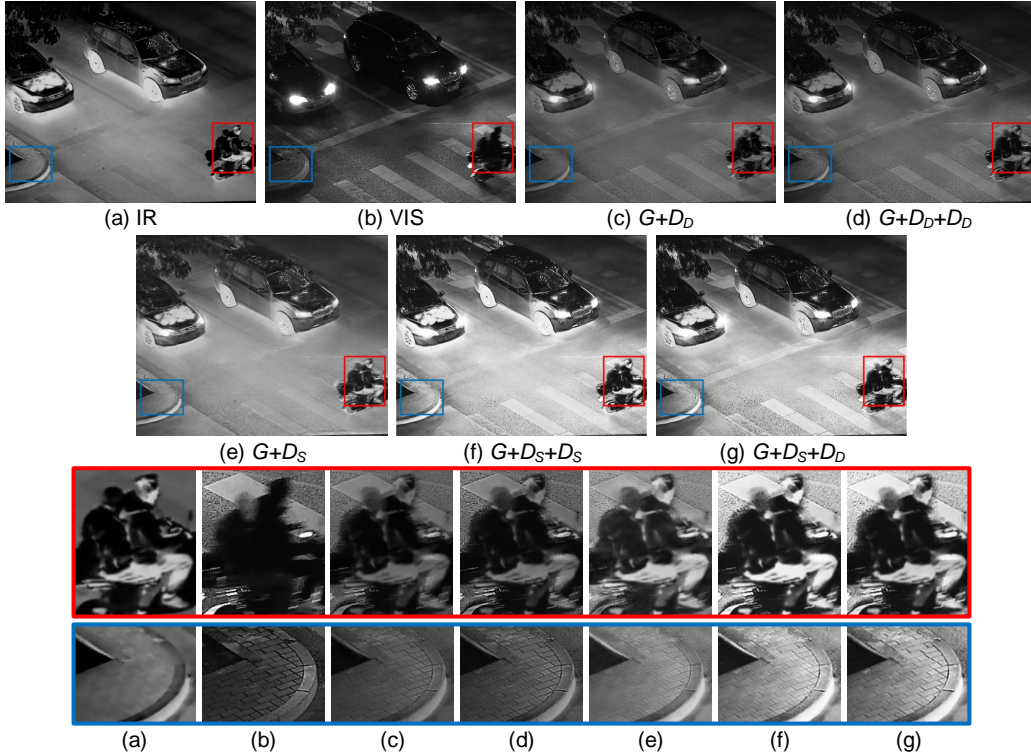


Fig. 11. Results for different discriminator structures on LLVIP.

thermal targets are not prominent enough, and the details lack clarity. In contrast, method (d), with the embedded MS-CA and MS-SA modules, not only retains rich information learned from the source image but also enhances the contrast and texture details. These results underscore the significance of the two attention modules in discriminators, showcasing their ability to improve the fusion effect further.

Ablation of \mathcal{D}_S and \mathcal{D}_D . AHDGAN comprises two distinct discriminators \mathcal{D}_S and \mathcal{D}_D . To elucidate the role of each discriminator and their effectiveness when applied, we conduct five sets of comparison experiments as depicted in Fig. 11 and Fig. 12. (a) and (b) represent the infrared and visible images, respectively. (c) discards the salient discriminator, employing only \mathcal{D}_D and G for the adversarial game. (d) incorporates detailed discriminators for both infrared and visible images. (e) removes the detailed discriminator,

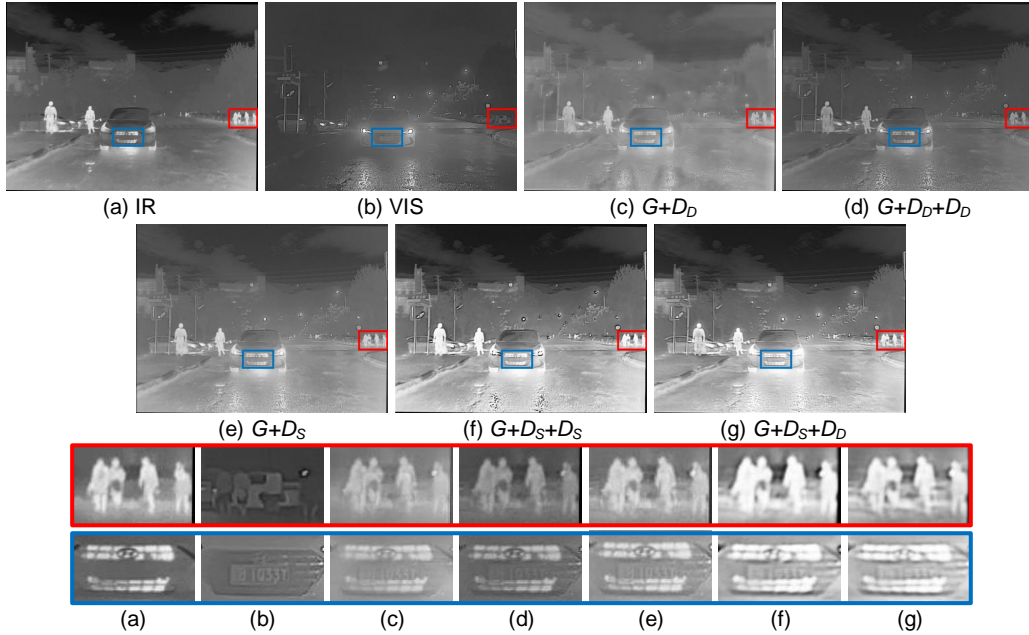


Fig. 12. Results for different discriminator structures on M^3FD .

establishing the adversarial game solely between \mathcal{D}_S and G . (f) utilizes the same salient discriminator for both infrared and visible images. (g) represents the structure embedded with \mathcal{D}_S and \mathcal{D}_D , identical to the setup employed in AHDGAN.

To facilitate clear comparisons, we zoom in on the selected thermal region information and texture detail information, respectively, as shown in the bottom red and blue boxes. Throughout the experiments, all parameters and environments remain constant, except for the variations mentioned above. Method (c) introduces \mathcal{D}_D , effectively preserving the textures displayed in the blue boxes, although the infrared information remains lost. Method (d) exhibits richer details after embedding both \mathcal{D}_D simultaneously. Method (e) adds \mathcal{D}_S on the basis of G , with the distribution of the fused image closer to the infrared image. However, the texture details in the blue boxes are poorly expressed. Method (f) presents more infrared information after introducing two \mathcal{D}_S , but the detailed information is not clear enough due to excessive brightness. Method (g) shares the same structure as AHDGAN, maintaining

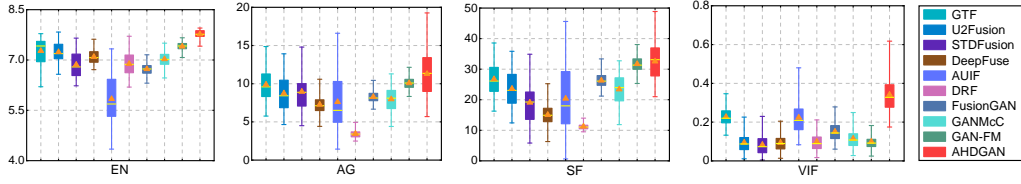


Fig. 13. Degradation analysis under noise scene on LLVIP. From left to right are EN, AG, SF, and VIF. In the boxes, the yellow lines and orange tangles indicate the median and mean values, respectively.

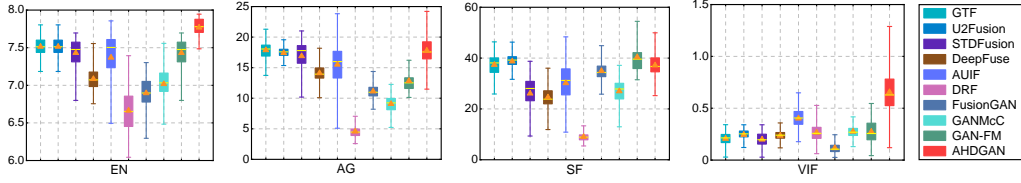


Fig. 14. Degradation analysis under noise scene on M^3FD . From left to right are EN, AG, SF, and VIF. The yellow lines and orange tangles indicate the median and mean values, respectively.

high contrast and preserving rich texture details by utilizing both \mathcal{D}_S and \mathcal{D}_D . These comparisons fully justify the use of these two distinct discriminators.

4.4. Degradation Resistance Experiment

As emphasized in [36], images captured by visible sensors are susceptible to environmental conditions, leading to potential visual degradation—an issue prevalent in practical application scenarios. IVIF technology emerges as a promising solution to mitigate such degradation by integrating information from infrared images. Thus, to delve deeper into the versatility of IVIF across various applications, we investigate the degradation resistance capabilities of several SOTA algorithms in this subsection.

Following the methodology outlined in [60], we introduce Gaussian noise with a variance σ of 0.03 to the visible images across all testing sets. We then evaluate the performance of various methods using four metrics on the LLVIP and M^3FD datasets. Fig. 13 and Fig. 14 present the noise resistance performance of different algorithms, revealing the overall effectiveness of AHDGAN.

Table 6

Comparison of target detection performance on LLVIP and M^3FD datasets with yolov5, the best two results are in red and blue fonts.

Datasets	Metrics	Infrared	Visible	GTF	U2Fusion	STDFusion	DeepFuse	AUIF	DRF	FusionGAN	GANMcC	GAN-FM	HDDGAN
LLVIP	Precision \uparrow	0.931	0.896	0.929	0.931	0.913	0.930	0.923	0.909	0.938	0.936	0.939	0.955
	Recall \uparrow	0.886	0.808	0.849	0.880	0.839	0.878	0.865	0.805	0.842	0.876	0.886	0.881
	mAP@.5 \uparrow	0.938	0.879	0.905	0.933	0.908	0.932	0.919	0.879	0.914	0.920	0.935	0.943
	mAP@.95 \uparrow	0.543	0.433	0.472	0.521	0.487	0.508	0.505	0.462	0.496	0.487	0.517	0.560
M^3FD	Precision \uparrow	0.788	0.814	0.793	0.796	0.811	0.802	0.774	0.860	0.775	0.778	0.742	0.815
	Recall \uparrow	0.525	0.525	0.547	0.585	0.543	0.570	0.575	0.500	0.531	0.557	0.599	0.603
	mAP@.5 \uparrow	0.567	0.597	0.603	0.645	0.614	0.639	0.641	0.589	0.587	0.615	0.627	0.666
	mAP@.95 \uparrow	0.317	0.335	0.359	0.385	0.358	0.383	0.381	0.348	0.353	0.361	0.374	0.406

4.5. Subsequent Application Verification

As mentioned earlier, IVIF combines thermal region information from infrared images with texture information from visible images, which is beneficial for improving the performance of visual tasks. And relative to other SOTA methods, AHDGAN can further emphasize key information. To verify this point, we apply the proposed model to object detection and visual tracking tasks and conduct comparative analyses with other algorithms.

1) *Object Detection*: Object detection is a widely employed machine vision technique [61] for detecting specific objects (people, cars, etc.) in images. Following [28], we use the well-known general-purpose detector YOLOv5 for object detection experiments on LLVIP and M^3FD . Table 6 reports the results of these two datasets. In this context, Precision denotes the probability of correctly detecting among all detected targets, and higher precision means more real samples are detected. Recall refers to the probability of correctly recognizing all positive samples, and a large recall means fewer targets are lost. The mean average precision (mAP) is a comprehensive consideration of Precision and Recall to evaluate the quality of the model. The value of mAP ranges from 0 to 1, and the closer the value is to 1, the better the model performs. The mAP@.5 and mAP@.95 denote the mAP values at confidence levels of 0.5 and 0.95, respectively. It is evident that the fusion results of AHDGAN excel in these metrics.

2) *Visual Tracking*: Visual tracking is also an essential task in computer vision, which aims to localize the position of specific objects in videos. Re-

Table 7

Tracking results for infrared frames, visible frames, and fused frames processed by 10 of the SOTA methods, the best two results are in red and blue fonts.

Tracker	Metrics	Infrared	Visible	GTF	U2Fusion	STDFusion	DeepFuse	AUIF	DRF	FusionGAN	GANMcC	GAN-FM	HDDGAN
LADCF	Accuracy \uparrow	0.5579	0.5099	0.4720	0.4072	0.4877	0.5636	0.5428	0.4166	0.5188	0.4668	0.4102	0.5934
	Failure \downarrow	58.9928	36.7437	63.2088	68.2383	57.7401	47.4615	47.2419	62.7696	41.0223	48.4960	73.4874	38.4946
	EAO \uparrow	0.1877	0.1970	0.2094	0.1602	0.1684	0.1848	0.1833	0.1780	0.1929	0.1757	0.1655	0.2234
GFSDCF	Accuracy \uparrow	0.5732	0.5253	0.5853	0.4382	0.4842	0.5751	0.5697	0.5243	0.5875	0.4900	0.4507	0.6270
	Failure \downarrow	54.4705	31.1229	45.7092	60.0464	52.7589	45.4410	45.2214	55.5957	38.1726	46.1970	60.2955	30.1482
	EAO \uparrow	0.2302	0.2498	0.2386	0.1834	0.1918	0.2260	0.2277	0.1988	0.2606	0.1999	0.1823	0.2541

ferring to [62], we apply the algorithm to the VOT-RGBT sub-challenge, which focuses on short-term tracking in VOT2020 to assess the impact of the fusion approach on tracking performance in a comparative manner. The VOT-RGBT benchmark, available in [63], comprises 60 video sequences with aligned infrared and visible image pairs. We select the learning adaptive discriminative correlation filter(LADCF) [64] and group feature selection and discriminative filter(GFSDCF) [65] as trackers for evaluating tracking performance. Among them, LADCF achieves the best performance in the public dataset of the VOT-ST2018 sub-challenge, while GFSDCF further eliminates redundant information based on LADCF through a group feature selection strategy. Their codes are publicly available. For quantitative analysis, we employ three metrics to evaluate tracking performance: Accuracy, Failure, and expected average overlap (EAO). Accuracy represents the average overlap between predicted bounding boxes and ground truth bounding boxes. Failure is a measure of tracker robustness. And EAO evaluates the average overlap in visual properties between the tracker and ground truth. Both Accuracy and EAO are the larger the better, while Failure is the smaller the better. The quantitative analysis is illustrated in Table 7. Compared with the metric values of infrared frames and visible frames, our fusion model has a positive impact on RGBT tracking. Furthermore, AHDGAN is more powerful in improving the performance of visual tracking compared to other fusion methods.

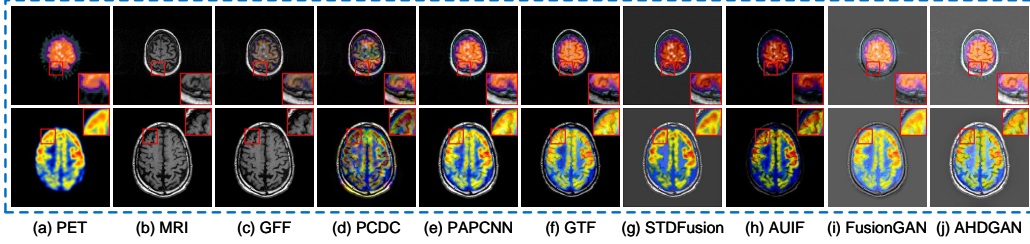


Fig. 15. Qualitative results of the medical image fusion task. From left to right, (a) and (b) are PET and MRI images, and (c)-(j) are GFF, PCDC, PAPCNN, GTF, STDFusion, AUIF, FusionGAN, and AHDGAN, respectively.

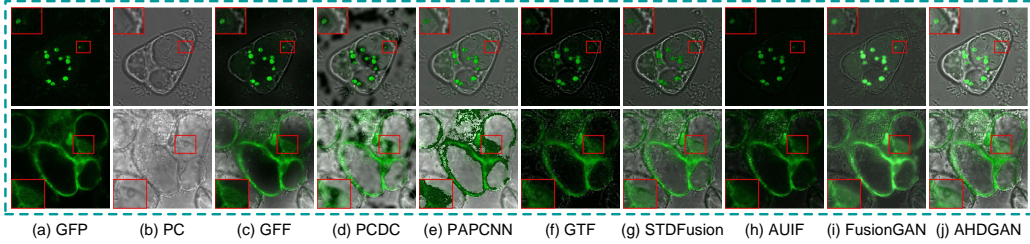


Fig. 16. Qualitative results of the biological image fusion task. From left to right, (a) and (b) are GFP and PC images, and (c)-(j) are GFF, PCDC, PAPCNN, GTF, STDFusion, AUIF, FusionGAN, and AHDGAN, respectively.

4.6. Extension of the Proposed AHDGAN

Since biomedical image fusion shares a similar goal with the IVIF task [66], we carry out two comparative experiments to assess the ability of our algorithm for the generalization in the spatial dimension. These tasks are PET and MRI image fusion (PET-MRI) and GFP and PC image fusion (GFP-PC). The images for the first task are sourced from the Whole Brain Atlas (WBA) [67], and the second task utilizes data from the ATC dataset [68]. Seven algorithms used for comparison, namely GFF [69], PCDC [70], PAPCNN [71], GTF, STDFusion, AUIF, and FusionGAN. Fig. 15 and Fig. 16 present the qualitative results of these methods, and it is easy to find that AHDGAN has better fusion outcomes compared to other methods that may suffer from detail distortion and color component preservation challenges. Besides, Table 8 and Table 9 also display the average results of these methods on six metrics, confirming that AHDGAN has good generalization performance compared to other methods.

Table 8

Quantitative analysis results for 259 images of the PET-MRI task, the best two results are in red and blue fonts.

Metrics	GFF	PCDC	PAPCNN	GTF	STDFusion	AUIF	FusionGAN	AHDGAN
EN \uparrow	4.075	4.216	4.221	3.468	4.254	3.026	3.935	4.805
AG \uparrow	5.952	5.929	5.973	4.914	5.391	2.954	3.232	5.980
SF \uparrow	25.665	25.371	25.320	22.362	22.603	15.065	12.874	25.680
FMI \uparrow	0.900	0.891	0.889	0.877	0.875	0.854	0.852	0.876
VIF \uparrow	0.493	0.367	0.637	0.446	0.259	0.365	0.265	0.505
UIQI \uparrow	0.907	0.821	0.922	0.753	0.498	0.534	0.454	0.639

Table 9

Quantitative analysis results for 147 images of the GFP-PC task, the best two results are in red and blue fonts.

Metrics	GFF	PCDC	PAPCNN	GTF	STDFusion	AUIF	FusionGAN	AHDGAN
EN \uparrow	6.554	6.536	6.628	4.798	6.494	4.147	5.960	6.914
AG \uparrow	3.724	3.791	4.976	2.472	4.590	1.266	2.955	5.045
SF \uparrow	9.580	8.498	16.073	6.485	11.114	4.745	7.158	12.811
FMI \uparrow	0.786	0.794	0.783	0.839	0.862	0.854	0.840	0.862
VIF \uparrow	0.074	0.090	0.091	0.259	0.486	0.156	0.314	0.760
UIQI \uparrow	0.735	0.849	0.855	0.240	0.817	0.272	0.605	0.897

5. Conclusion

In this study, we propose a novel model called attention-based generator and heterogeneous dual-discriminator GAN. Benefiting from these heterogeneous discriminators, our model is capable of learning more features from different source images in a targeted manner, especially the important information. Moreover, we design a fusion module named attention-based fusion strategy within the generator, which can realize a reasonable characterization of the acquired information during the fusion process. Various experiments conducted on numerous public datasets fully demonstrate the superiority and robustness of AHDGAN, as well as its potential for practical applications. In our future work, we will further explore a more lightweight and generalized fusion model based on the strengths of AHDGAN.

Acknowledgments

This research was supported by Horizontal Scientific Research Project of Shenzhen Technology University (No. 20231064010094, No. 20231064010029, No. 20241064010018), Graduate School-Enterprise Cooperation Project of Shenzhen Technology University (No. XQHZ202304, No. XQHZ2024006).

References

- [1] Z. Pan, H. Lin, Q. Wu, G. Xu, Q. Yu, Residual texture-aware infrared and visible image fusion with feature selection attention and adaptive loss, *Infrared Physics & Technology* (2024) 105410.
- [2] J. Xiong, G. Liu, H. Tang, X. Gu, D. P. Bavirisetti, Segfusion: A semantic saliency guided infrared and visible image fusion method, *Infrared Physics & Technology* 140 (2024) 105344.
- [3] H. Chi, D. Luo, S. Wang, Lmdfusion: A lightweight infrared and visible image fusion network for substation equipment based on mask and residual dense connection, *Infrared Physics & Technology* 138 (2024) 105218.
- [4] H. Zhang, J. Yuan, X. Tian, J. Ma, Gan-fm: Infrared and visible image fusion using gan with full-scale skip connection and dual markovian discriminators, *IEEE Transactions on Computational Imaging* 7 (2021) 1134–1147.
- [5] L. Liang, X. Shen, Z. Gao, Ifici: Infrared and visible image fusion based on interactive compensation illumination, *Infrared Physics & Technology* 136 (2024) 105078.
- [6] P. J. Burt, E. H. Adelson, The laplacian pyramid as a compact image code, in: *Readings in computer vision*, Elsevier, 1987, pp. 671–679.
- [7] C. He, X. Wang, L. Deng, G. Xu, Image threshold segmentation based on gll histogram, in: *CPSCoM*, IEEE, 2019, pp. 410–415.

- [8] J. J. Lewis, R. J. O’Callaghan, S. G. Nikolov, D. R. Bull, N. Canagarajah, Pixel-and region-based image fusion with complex wavelets, *Information fusion* 8 (2) (2007) 119–130.
- [9] Q. Zhang, T. Shi, F. Wang, R. S. Blum, J. Han, Robust sparse representation based multi-focus image fusion with dictionary construction and local spatial consistency, *Pattern Recognition* 83 (2018) 299–313.
- [10] J. Wang, J. Peng, X. Feng, G. He, J. Fan, Fusion method for infrared and visible images by using non-negative sparse representation, *Infrared Physics & Technology* 67 (2014) 477–489.
- [11] Y. Zheng, E. A. Essock, B. C. Hansen, An advanced image fusion algorithm based on wavelet transform: incorporation with pca and morphological processing, in: *Image processing: algorithms and systems III*, Vol. 5298, SPIE, 2004, pp. 177–187.
- [12] Y. Liu, S. Liu, Z. Wang, A general framework for image fusion based on multi-scale transform and sparse representation, *Information fusion* 24 (2015) 147–164.
- [13] C. He, K. Li, Y. Zhang, G. Xu, L. Tang, Y. Zhang, Z. Guo, X. Li, Weakly-supervised concealed object segmentation with sam-based pseudo labeling and multi-scale feature grouping, *arXiv preprint [arXiv:2305.11003](https://arxiv.org/abs/2305.11003)* (2023).
- [14] H. Xu, J. Ma, J. Jiang, X. Guo, H. Ling, U2fusion: A unified unsupervised image fusion network, *IEEE Transactions on Pattern Analysis and Machine Intelligence* 44 (1) (2020) 502–518.
- [15] F. Xiao, P. Zhang, C. He, R. Hu, Y. Liu, Concealed object segmentation with hierarchical coherence modeling, in: *CAAI*, Springer, 2023, pp. 16–27.

- [16] L. Tang, K. Li, C. He, Y. Zhang, X. Li, Source-free domain adaptive fundus image segmentation with class-balanced mean teacher, in: MICCAI, Springer, 2023, pp. 684–694.
- [17] M. Ju, C. He, J. Liu, B. Kang, J. Su, D. Zhang, Ivf-net: An infrared and visible data fusion deep network for traffic object enhancement in intelligent transportation systems, *IEEE Transactions on Intelligent Transportation Systems* 24 (1) (2022) 1220–1234.
- [18] Y. Zhang, Y. Liu, P. Sun, H. Yan, X. Zhao, L. Zhang, Ifcnn: A general image fusion framework based on convolutional neural network, *Information Fusion* 54 (2020) 99–118.
- [19] H. Li, X.-J. Wu, Densefuse: A fusion approach to infrared and visible images, *IEEE Transactions on Image Processing* 28 (5) (2018) 2614–2623.
- [20] L. Tang, K. Li, C. He, Y. Zhang, X. Li, Consistency regularization for generalizable source-free domain adaptation, in: ICCV, 2023, pp. 4323–4333.
- [21] L. Xu, H. Wu, C. He, J. Wang, C. Zhang, F. Nie, L. Chen, Multi-modal sequence learning for alzheimer’s disease progression prediction with incomplete variable-length longitudinal data, *Medical Image Analysis* 82 (2022) 102643.
- [22] Z. Wang, J. Wang, Y. Wu, J. Xu, X. Zhang, Unfusion: A unified multi-scale densely connected network for infrared and visible image fusion, *IEEE Transactions on Circuits and Systems for Video Technology* 32 (6) (2021) 3360–3374.
- [23] J. Ma, W. Yu, P. Liang, C. Li, J. Jiang, FusionGAN: A generative adversarial network for infrared and visible image fusion, *Information fusion* 48 (2019) 11–26.

- [24] J. Ma, H. Xu, J. Jiang, X. Mei, X.-P. Zhang, Ddcgan: A dual-discriminator conditional generative adversarial network for multi-resolution image fusion, *IEEE Transactions on Image Processing* 29 (2020) 4980–4995.
- [25] J. Ma, H. Zhang, Z. Shao, P. Liang, H. Xu, Ganmcc: A generative adversarial network with multiclassification constraints for infrared and visible image fusion, *IEEE Transactions on Instrumentation and Measurement* 70 (2020) 1–14.
- [26] J. Li, H. Huo, C. Li, R. Wang, Q. Feng, Attentionfgan: Infrared and visible image fusion using attention-based generative adversarial networks, *IEEE Transactions on Multimedia* 23 (2020) 1383–1396.
- [27] J. Li, H. Huo, C. Li, R. Wang, C. Sui, Z. Liu, Multigrained attention network for infrared and visible image fusion, *IEEE Transactions on Instrumentation and Measurement* 70 (2020) 1–12.
- [28] J. Liu, X. Fan, Z. Huang, G. Wu, R. Liu, W. Zhong, Z. Luo, Target-aware dual adversarial learning and a multi-scenario multi-modality benchmark to fuse infrared and visible for object detection, in: *Proceedings of the IEEE/CVF Conference on Computer Vision and Pattern Recognition*, 2022, pp. 5802–5811.
- [29] L. Deng, C. He, G. Xu, H. Zhu, H. Wang, Pcgan: A noise robust conditional generative adversarial network for one shot learning, *IEEE Transactions on Intelligent Transportation Systems* 23 (12) (2022) 25249–25258.
- [30] C. He, K. Li, G. Xu, J. Yan, L. Tang, Y. Zhang, Y. Wang, X. Li, Hqgnet: Unpaired medical image enhancement with high-quality guidance, *IEEE Transactions on Neural Networks and Learning Systems* (2023).
- [31] F. Nencini, A. Garzelli, S. Baronti, L. Alparone, Remote sensing image

- fusion using the curvelet transform, *Information fusion* 8 (2) (2007) 143–156.
- [32] Y. Liu, X. Chen, R. K. Ward, Z. J. Wang, Image fusion with convolutional sparse representation, *IEEE signal processing letters* 23 (12) (2016) 1882–1886.
- [33] C. He, K. Li, Y. Zhang, L. Tang, Y. Zhang, Z. Guo, X. Li, Camouflaged object detection with feature decomposition and edge reconstruction, in: *Proceedings of the IEEE/CVF Conference on Computer Vision and Pattern Recognition, 2023*, pp. 22046–22055.
- [34] N. Cvejic, D. Bull, N. Canagarajah, Region-based multimodal image fusion using ica bases, *IEEE Sensors Journal* 7 (5) (2007) 743–751.
- [35] C. He, K. Li, Y. Zhang, Y. Zhang, Z. Guo, X. Li, M. Danelljan, F. Yu, Strategic preys make acute predators: Enhancing camouflaged object detectors by generating camouflaged objects, *arXiv preprint [arXiv:2308.03166](https://arxiv.org/abs/2308.03166)* (2023).
- [36] J. Ma, C. Chen, C. Li, J. Huang, Infrared and visible image fusion via gradient transfer and total variation minimization, *Information Fusion* 31 (2016) 100–109.
- [37] Y. Liu, X. Chen, H. Peng, Z. Wang, Multi-focus image fusion with a deep convolutional neural network, *Information Fusion* 36 (2017) 191–207.
- [38] H. Li, X.-j. Wu, T. S. Durrani, Infrared and visible image fusion with resnet and zero-phase component analysis, *Infrared Physics & Technology* 102 (2019) 103039.
- [39] H. Li, X.-J. Wu, T. Durrani, Nestfuse: An infrared and visible image fusion architecture based on nest connection and spatial/channel attention models, *IEEE Transactions on Instrumentation and Measurement* 69 (12) (2020) 9645–9656.

- [40] H. Zhou, W. Wu, Y. Zhang, J. Ma, H. Ling, Semantic-supervised infrared and visible image fusion via a dual-discriminator generative adversarial network, *IEEE Transactions on Multimedia* (2021).
- [41] Q. Wang, B. Wu, P. Zhu, P. Li, W. Zuo, Q. Hu, Eca-net: Efficient channel attention for deep convolutional neural networks, in: *Proceedings of the IEEE/CVF conference on computer vision and pattern recognition*, 2020, pp. 11534–11542.
- [42] B. Zhou, A. Khosla, A. Lapedriza, A. Oliva, A. Torralba, Learning deep features for discriminative localization, in: *Proceedings of the IEEE conference on computer vision and pattern recognition*, 2016, pp. 2921–2929.
- [43] P. Isola, J.-Y. Zhu, T. Zhou, A. A. Efros, Image-to-image translation with conditional adversarial networks, in: *Proceedings of the IEEE conference on computer vision and pattern recognition*, 2017, pp. 1125–1134.
- [44] Y. Liu, Z. Shao, N. Hoffmann, Global attention mechanism: Retain information to enhance channel-spatial interactions, *arXiv preprint [arXiv:2112.05561](https://arxiv.org/abs/2112.05561)* (2021).
- [45] H. Zhang, H. Xu, X. Tian, J. Jiang, J. Ma, Image fusion meets deep learning: A survey and perspective, *Information Fusion* 76 (2021) 323–336.
- [46] C. He, C. Fang, Y. Zhang, K. Li, L. Tang, C. You, F. Xiao, Z. Guo, X. Li, Reti-diff: Illumination degradation image restoration with retinex-based latent diffusion model, *arXiv preprint [arXiv:2311.11638](https://arxiv.org/abs/2311.11638)* (2023).
- [47] X. Jia, C. Zhu, M. Li, W. Tang, W. Zhou, Llvip: A visible-infrared paired dataset for low-light vision, in: *Proceedings of the IEEE/CVF international conference on computer vision*, 2021, pp. 3496–3504.

- [48] J. Ma, L. Tang, M. Xu, H. Zhang, G. Xiao, Stdfusionnet: An infrared and visible image fusion network based on salient target detection, *IEEE Transactions on Instrumentation and Measurement* 70 (2021) 1–13.
- [49] K. Ram Prabhakar, V. Sai Srikar, R. Venkatesh Babu, Deepfuse: A deep unsupervised approach for exposure fusion with extreme exposure image pairs, in: *Proceedings of the IEEE international conference on computer vision*, 2017, pp. 4714–4722.
- [50] Z. Zhao, S. Xu, J. Zhang, C. Liang, C. Zhang, J. Liu, Efficient and model-based infrared and visible image fusion via algorithm unrolling, *IEEE Transactions on Circuits and Systems for Video Technology* 32 (3) (2021) 1186–1196.
- [51] H. Xu, X. Wang, J. Ma, Drf: Disentangled representation for visible and infrared image fusion, *IEEE Transactions on Instrumentation and Measurement* 70 (2021) 1–13.
- [52] G. Xu, C. He, H. Wang, H. Zhu, W. Ding, Dm-fusion: Deep model-driven network for heterogeneous image fusion, *IEEE Transactions on Neural Networks and Learning Systems* (2023).
- [53] C. He, K. Li, G. Xu, Y. Zhang, R. Hu, Z. Guo, X. Li, Degradation-resistant unfolding network for heterogeneous image fusion, in: *Proceedings of the IEEE/CVF International Conference on Computer Vision*, 2023, pp. 12611–12621.
- [54] J. W. Roberts, J. A. Van Aardt, F. B. Ahmed, Assessment of image fusion procedures using entropy, image quality, and multispectral classification, *Journal of Applied Remote Sensing* 2 (1) (2008) 023522.
- [55] H. Li, Y. Cen, Y. Liu, X. Chen, Z. Yu, Different input resolutions and arbitrary output resolution: A meta learning-based deep framework for infrared and visible image fusion, *IEEE Transactions on Image Processing* 30 (2021) 4070–4083.

- [56] S. Li, J. T. Kwok, Y. Wang, Combination of images with diverse focuses using the spatial frequency, *Information fusion* 2 (3) (2001) 169–176.
- [57] M. B. A. Haghighat, A. Aghagolzadeh, H. Seyedarabi, A non-reference image fusion metric based on mutual information of image features, *Computers & Electrical Engineering* 37 (5) (2011) 744–756.
- [58] Y. Han, Y. Cai, Y. Cao, X. Xu, A new image fusion performance metric based on visual information fidelity, *Information fusion* 14 (2) (2013) 127–135.
- [59] Z. Wang, A. C. Bovik, A universal image quality index, *IEEE signal processing letters* 9 (3) (2002) 81–84.
- [60] W. Yang, R. T. Tan, J. Feng, J. Liu, Z. Guo, S. Yan, Deep joint rain detection and removal from a single image, in: *Proceedings of the IEEE conference on computer vision and pattern recognition*, 2017, pp. 1357–1366.
- [61] L. Liu, W. Ouyang, X. Wang, P. Fieguth, J. Chen, X. Liu, M. Pietikäinen, Deep learning for generic object detection: A survey, *International journal of computer vision* 128 (2020) 261–318.
- [62] H. Li, X.-J. Wu, J. Kittler, Mdlatlr: A novel decomposition method for infrared and visible image fusion, *IEEE Transactions on Image Processing* 29 (2020) 4733–4746.
- [63] M. Kristan, J. Matas, A. Leonardis, M. Felsberg, R. Pflugfelder, J.-K. Kamarainen, L. Čehovin Zajc, O. Drbohlav, A. Lukežič, A. Berg, et al., The seventh visual object tracking vot2019 challenge results, in: *Proceedings of the IEEE/CVF international conference on computer vision workshops*, 2019, pp. 0–0.
- [64] T. Xu, Z.-H. Feng, X.-J. Wu, J. Kittler, Learning adaptive discriminative correlation filters via temporal consistency preserving spatial feature

- selection for robust visual object tracking, *IEEE Transactions on Image Processing* 28 (11) (2019) 5596–5609.
- [65] T. Xu, Z.-H. Feng, X.-J. Wu, J. Kittler, Joint group feature selection and discriminative filter learning for robust visual object tracking, in: *Proceedings of the IEEE/CVF international conference on computer vision*, 2019, pp. 7950–7960.
- [66] A. P. James, B. V. Dasarathy, Medical image fusion: A survey of the state of the art, *Information fusion* 19 (2014) 4–19.
- [67] J. A. Johnson, J. A. Becker, *The whole brain atlas* (1997).
- [68] O. A. Koroleva, M. L. Tomlinson, D. Leader, P. Shaw, J. H. Doonan, High-throughput protein localization in arabidopsis using agrobacterium-mediated transient expression of gfp-orf fusions, *The Plant Journal* 41 (1) (2005) 162–174.
- [69] S. Li, X. Kang, J. Hu, Image fusion with guided filtering, *IEEE Transactions on Image processing* 22 (7) (2013) 2864–2875.
- [70] G. Bhatnagar, Q. J. Wu, Z. Liu, Directive contrast based multimodal medical image fusion in nsct domain, *IEEE transactions on multimedia* 15 (5) (2013) 1014–1024.
- [71] M. Yin, X. Liu, Y. Liu, X. Chen, Medical image fusion with parameter-adaptive pulse coupled neural network in nonsampled shearlet transform domain, *IEEE Transactions on Instrumentation and Measurement* 68 (1) (2018) 49–64.